

Crystallization and grain growth characteristics of yttria-stabilized zirconia thin films grown by pulsed laser deposition

Sebastian Heiroth^a, Ruggero Frison^b, Jennifer L.M. Rupp^c, Thomas Lippert^{a,*}, Eszter J. Barthazy Meier^d, Elisabeth Müller Gubler^d, Max Döbeli^e, Kazimierz Conder^b, Alexander Wokaun^a, Ludwig J. Gauckler^c

^a General Energy Research Department, Paul Scherrer Institut, 5232 Villigen-PSI, Switzerland

^b Laboratory for Development and Methods, Paul Scherrer Institut, 5232 Villigen-PSI, Switzerland

^c Nonmetallic Inorganic Materials, Department of Materials, Swiss Federal Institute of Technology, ETH Zurich, Wolfgang Pauli Str. 10, 8093 Zurich, Switzerland

^d Electron Microscopy ETH Zurich (EMEZ), Swiss Federal Institute of Technology, ETH Zurich, Wolfgang Pauli Str. 16, 8093 Zurich, Switzerland

^e Ion Beam Physics, ETH Zurich, 8093 Zurich, Switzerland

ARTICLE INFO

Article history:

Received 14 November 2010

Received in revised form 10 April 2011

Accepted 11 April 2011

Available online 5 May 2011

Keywords:

Crystallization

Grain growth

Ceramics

Thin films

Yttria-stabilized zirconia

Pulsed laser deposition

ABSTRACT

Knowledge about the crystallization and grain growth characteristics of metal oxide thin films is essential for effective microstructural engineering by thermal post-annealing and the integration to Si-based miniaturized electroceramic devices. Finite size and interface effects may cause fundamentally different behavior compared to three dimensional macroscopic systems. This work presents a comprehensive investigation of the crystallization kinetics and microstructural evolution upon thermal post-annealing of amorphous 200 nm and 1.2 μm thin films of 8 mol% yttria-stabilized zirconia grown by pulsed laser deposition (PLD) using ex- and in-situ X-ray diffraction, Raman spectroscopy, and electron microscopy techniques. The layers exhibit a remarkably low crystallization temperature of 200–250 °C while exposure to energetic electrons induces the formation of randomly dispersed ~20 nm sized crystallites already at ambient temperature. The isothermal amorphous to crystalline phase transformation kinetics can be described quantitatively by the Johnson–Mehl–Avrami–Kolmogorov model. They reveal characteristics of a three dimensional growth under cation bulk diffusion control with heterogeneous nucleation that changes from continuous to instantaneous initial seeding at temperatures above 300 °C. Large (>100 nm) equiaxed grains are formed rapidly without a stabilization of transient nanocrystals during the thermally induced phase transformation. A stagnation of normal grain growth resulting in a logarithmic normal size distribution is observed once the average grain dimensions approach the film thickness. The results on the crystallization and grain growth of the PLD-grown YSZ films are evaluated with regards to the fabrication of YSZ solid electrolyte membranes for Si-supported micro solid oxide fuel cells and gas sensors.

© 2011 Elsevier B.V. All rights reserved.

1. Introduction

The integration of electroceramic metal oxide films represents a key issue in the thriving field of microelectromechanical systems (MEMS) technology for the development of miniaturized electromechanical and electro optical devices, sensors, and energy converters [1]. The major challenge derives from the incompatibility of the established Si-based microfabrication with the high temperatures applied in conventional ceramic fabrication techniques. ‘Soft’ processing routes that minimize the thermal stresses caused by the mismatch of thermal expansion coefficients as well as the thermal degradation

by interdiffusion or interfacial chemical reactions with the substrate respectively adjacent layers are required.

The strong non-equilibrium conditions in pulsed laser deposition (PLD) or sputtering inherently favor for instance the growth of crystalline films at comparatively moderate temperatures, typically ~500–600 °C [2]. Modifications such as the application of an electrical bias [3], a magnetic field [4], or a lattice matching seed layer [5] further decrease the required deposition temperatures.

At ambient temperature these physical vapor deposition (PVD) techniques as well as chemical precipitation methods such as sol–gel, spin or dip coating or spray pyrolysis commonly yield amorphous layers [6]. The amorphous films can be crystallized by post-annealing, frequently resulting in microstructures, which are very different to the direct deposition of a crystalline layer at elevated temperature. The microstructure, in particular the grain size and the degree of crystallinity affect the films’ electrical, optical and catalytic properties significantly [7–10]. Knowledge on the crystallization characteristics and the thermal microstructural evolution is thus essential for the

* Corresponding author. Tel.: +41 56 3104076; fax: +41 56 3102688.

E-mail addresses: sebastian.heiroth@psi.ch (S. Heiroth), ruggero.frison@psi.ch (R. Frison), jennifer.rupp@mat.ethz.ch (J.L.M. Rupp), thomas.lippert@psi.ch (T. Lippert), eszter.barthazy@emez.ethz.ch (E.J. Barthazy Meier), elisabeth.mueller@emez.ethz.ch (E. Müller Gubler), doebeli@phys.ethz.ch (M. Döbeli), kazimierz.conder@psi.ch (K. Conder), alexander.wokaun@psi.ch (A. Wokaun), ludwig.gauckler@mat.ethz.ch (L.J. Gauckler).

development of ‘soft’ thin film deposition routes and effective microstructural engineering. However, despite of their technological relevance, the crystallization and grain growth of electroceramic metal oxide layers has been studied only scarcely with a clear focus on piezoelectric lead zirconate titanate (PZT) films [11–14] and recent reports about ceria-based films [15,16].

Thin films of yttria-stabilized zirconia (YSZ) as the most important solid electrolyte material have been prepared by a variety of different techniques including spin coating [17], r.f. sputtering [18], pulsed laser deposition [19–21], chemical vapor deposition [22], and spray pyrolysis [23]. Nevertheless, the crystallization characteristics of the material have been studied intensively only for gels and powders obtained from wet chemistry techniques [24–29]. In these cases the phase transformation occurs consistently at temperatures in the range of 400–500 °C, subsequent to solvent evaporation at lower temperatures. As a result tetragonal (≤ 7 mol% Y_2O_3) [24,25] or cubic (≥ 8 mol% Y_2O_3) [27,29] zirconia with nanocrystalline grain dimensions (≤ 100 nm) is formed. A significant scatter beyond the effect of variations in the yttria content [28] exists in the reported crystallization activation energies with values ranging from 27 kJ/mol [26] to 232 kJ/mol [27]. Furthermore, kinetic studies yield no consistent mechanistic view as interpretations vary from a three [25,27] or two [29] dimensional diffusion controlled growth to a diffusionless transformation with interfacial control [26]. These differences are probably related to the different incorporated chemical species as well as the varying agglomeration and near range order within the precursor material prepared by the distinct precipitation routes [30].

The few publications on the crystallization of amorphous YSZ thin films focus mainly on the effects of thermal post annealing on the electrical properties of the layers [21,31,32]. Kiguchi et al. [33] give rare mechanistic insights observing heterogeneous nucleation close to the film surface and subsequent grain growth with strain accommodation at the film/substrate interface for YSZ/Si and YSZ/ SiO_x /Si systems by high temperature in-situ TEM. However, a detailed and systematic investigation of the crystallization and grain growth characteristics of YSZ thin films, in particular a quantitative analysis of the kinetics, is clearly missing so far.

The kinetics of isothermal phase transitions proceeding via nucleation and growth are described by the Johnson–Mehl–Avrami–Kolmogorov (JMAK) model [34–36], which yields the transformed volume fraction as a function of the dwell time, $x(t)$, as

$$x(t) = 1 - \exp(-kt^n) \quad (1)$$

Herein, n is the Avrami exponent, which depends on the nucleation and growth mode, and k is the rate constant given by

$$k(T) = A \cdot \exp\left(\frac{-Q}{k_b T}\right) \quad (2)$$

where Q represents the activation energy, k_b is the Boltzmann constant, and A is a pre-exponential factor.

While the crystallization process is driven by the difference in the chemical potential between the amorphous and the crystalline phase, grain growth in the resulting polycrystalline material is driven by the minimization of the total grain boundary area.

Grain growth in bulk, three dimensional systems is usually described by a power law function [37]

$$D^m - D_0^m = qt \quad (3)$$

where D represents the mean grain size at a time t , D_0 is the initial average grain size while the proportionality constant, q , is related to the grain boundary mobility and energy. Burke and Turnbull showed that a growth exponent of $m=2$ is expected theoretically, which relates the isothermal grain growth rate, dD/dt , to the mean radius of

grain curvature [38]. However, experimental values of the growth exponent in the range of 2–10 have been reported [39]. Deviations from parabolic grain growth ($m=2$) have been attributed to different drag forces, i.e. a reduction of the grain boundary mobility by triple junctions [40], precipitates [41] and pores or solute respectively impurity segregation to the grain boundaries [42,43].

Normal grain growth of bulk microcrystalline YSZ, which was found to follow the classical behavior with a growth exponent of $m=3$ and an activation energy of 580 kJ/mol [44], is generally accepted to be controlled by the solute drag resulting from Y^{3+} segregation to the grain boundaries [45]. Nanocrystalline sol-gel derived powders reveal significantly lower activation energies as small as ~ 13 kJ/mol [46], and may exhibit abnormal grain growth modes [47].

In the case of thin films, a stagnation of normal grain growth is often observed once the mean grain dimensions approach the order of the layer thickness [37,48]. Mullins et al. [49] related this specimen thickness effect to a drag force of grain boundary grooves formed at the film surface. Limited grain growth was also observed by Dong et al. [50] for 8 mol% yttria-doped zirconia films derived by spin coating from polymeric precursors. However, in this case nanocrystalline microstructures with grain sizes <30 nm, i.e. well below the layer thickness of 120 nm, were stabilized at intermediate temperatures of up to 1000 °C. Similarly, Rupp et al. [39] reported self-limited grain growth kinetics for initially amorphous ceria-based thin films prepared by spray pyrolysis with a transition to classical curvature-driven growth at temperatures above 1100 °C. The inhibition of grain coarsening was attributed to elastic strain in amorphous phase residuals and to carbon impurities detected at temperatures of up to 1000 °C [16,51].

This evidence and the inconsistent mechanistic view for the crystallization of precipitation-based YSZ powders and gels emphasize the strong influence that the choice of precursors and solvents may have on the phase transformation and grain growth in the case of wet chemistry based synthesis. These influences can be eliminated by using thin films deposited by PVD techniques, which are solvent-free and contain only a low level of impurities, as ideal model systems to study the crystallization and grain growth behavior of the pure metal oxide.

In our previous work we have demonstrated that dense amorphous YSZ thin films can be prepared by PLD at ambient temperature [52,53]. This study aims at a detailed investigation of the phase, microstrain, and grain size evolution upon thermal post-annealing of the amorphous PLD-grown YSZ films. The phase transformation kinetics are determined and discussed with respect to crystallization and grain growth literature on thin films and powders. The experimental results are assessed from the perspective of microstructural engineering and device integration of YSZ thin films for substrate supported solid electrolyte membranes in micro solid oxide fuel cells [54,55], Nernstian gas sensors [56] or oxygen separation membranes [57].

2. Experimental

2.1. Thin film deposition

Two sets of YSZ layers with a thickness of 200 ± 10 nm respectively 1200 ± 30 nm were grown by pulsed laser deposition on $10 \text{ mm} \times 10 \text{ mm} \times 0.5 \text{ mm}$ c-cut sapphire single crystal substrates (Crystec GmbH) in a high vacuum chamber. A rotating ceramic target, produced by pressing of 8 mol% Y_2O_3 -doped ZrO_2 powder (Tosoh Corp.) at 4.0 kbar and subsequent sintering for 10 h at 1600 °C, was ablated by a KrF excimer laser (λ : 248 nm, τ : 20 ns, repetition rate: 10 Hz) incident at an angle of 45°. A homogeneous central part of the beam was cut by an aperture ($5.0 \text{ mm} \times 5.0 \text{ mm}$) and projected onto the target surface by a UV-grade fused silica lens (f : +500 mm), yielding a spot size of 1.0 mm^2

and a fluence of 1.5–1.7 J/cm² using an imaging setup. The ablated material was deposited at normal incidence on a substrate mounted on a rotary sample holder positioned in a distance of 40 mm to the target. All depositions were conducted in an oxygen background atmosphere at a fixed pressure of 1.0 Pa without additional heating of the substrate, yielding dense and smooth amorphous YSZ films [52,53]. The actual temperature of the substrate that is heated by the incident plasma plume does not exceed 70 °C as measured by a thermocouple, which was bonded to its surface. The layer thicknesses were measured with a stylus-type Dektak 8 surface profilometer (Veeco Inc.).

2.2. Thin film crystallization studies

The as-deposited layers were annealed ex-situ in a tubular furnace in static air at different peak temperatures in the range of 150–1000 °C using a maximum dwell time of 20 h and a constant heating and cooling rate of 3 K/min to investigate the microstructural changes upon thermal treatment. The crystallographic phase composition and texture were analyzed by X-ray diffraction employing a Bruker AXS D8 Advance instrument in Bragg–Brentano geometry equipped with a position sensitive detector. The Cu radiation source yielded Cu K_α radiation (λ: 1.5418 Å), while K_β contributions were eliminated by a Ni-filter. Diffraction patterns were detected in symmetric scan mode in a 2θ-range of 25–90° using an incremental step width of 0.01° and an integration time of 5 s/step.

The isothermal crystallization kinetics of the as-deposited amorphous 8YSZ layers were studied in-situ at different dwell temperatures up to 450 °C in vacuum using a heating stage (Anton Paar TTK 450) mounted to the diffractometer. A heating rate of 30 K/min was applied. Diffraction patterns were detected as a function of annealing time at the set peak temperature in a limited 2θ-range of 29–31°, the region of the most intense (111) reflection, at a fast rate of 0.2 s/step, yielding a reasonable temporal resolution with an acquisition time of ~45 s for a single measurement.

The (0006) reflection of the sapphire single crystal substrates at 2θ = 41.685° was utilized as an internal reference in the ex- and in-situ XRD experiments to correct for slight deviations of the sample height from the instrumental reference level within the EVA analysis software. The peaks were fitted by a Voigt function [58].

The lattice parameter of the cubic YSZ lattice, *a*, was calculated as an average value from the angular positions of the peak maxima according to [59]

$$a = \frac{\lambda \sqrt{h^2 + k^2 + l^2}}{2 \sin \theta} \quad (4)$$

Herein, *θ* denotes the diffraction angle (in radians), *λ* represents the wavelength of the radiation and *h*, *k* and *l* are the Miller indices of the respective Bragg reflection.

The crystallographic density, *ρ*, is derived from the lattice parameter by [59]

$$\rho = \frac{Z \cdot M}{a^3 \cdot N_A} \quad (5)$$

where *Z* represents the number of formula units per unit cell, *M* is the molar mass and *N_A* is Avogadro's number.

The experimental full width at half maximum (FWHM), Δ(2θ)_{exp}, was corrected for the instrumental contribution to peak broadening, (Δ2θ)_i, which was determined by measuring a stress-free Na₂Al₂Ca₃F₁₄ powder standard, according to [60]

$$\Delta(2\theta)_c^2 = \Delta(2\theta)_{exp}^2 - \Delta(2\theta)_i^2 \quad (6)$$

The angular variance of the corrected FWHM, Δ(2θ)_c, was analyzed for the ex-situ annealed films following the procedure introduced by

Williamson and Hall to determine the microstrain, *ε*, and average grain size, *D*, from plots of Δ(2θ)_c · cos*θ* versus sin*θ* based on Eq. (7) [60].

$$\Delta(2\theta)_c \cdot \cos \theta = \frac{\lambda}{D} + 2\varepsilon \cdot \sin \theta \quad (7)$$

The temporal progress of the crystallization process during the isothermal in-situ XRD experiments can be expressed as the film's volume fraction, *x(t)*, which was transformed from the amorphous to the crystalline phase within the time *t*. The transformed volume fraction was deduced from the integrated peak area, *A(t)*, which is directly proportional to the amount of diffracting crystalline material, according to

$$x(t) = \frac{A(t)}{A_f} \quad (8)$$

where *A_f* is the integrated peak area after complete crystallization [26], i.e. in the case of the YSZ layers the constant peak area value attained after a maximum of 20 h.

Additional information about the film phase composition as a function of the applied ex-situ annealing temperature was derived by Raman spectroscopy employing a Raman microscope (LabRAM Series, Horiba Jobin Yvon) with a He–Ne excitation laser (λ: 632.8 nm, output power: ~10 mW) focused to probe an analyte volume of ~1 μm³. For Raman analysis YSZ layers deposited as described above on 5.0 mm × 5.0 mm × 0.5 mm LaAlO₃ (110) single crystals were selected to avoid the severe superposition of film and substrate peaks, which obscures the interpretation of the spectra in the case of sapphire substrates.

The film microstructure and grain growth were analyzed by electron microscopy. Grain size distributions were obtained from top view scanning electron microscopy (SEM) images, acquired with a Zeiss Supra VP55 FE-SEM, by Heyn's mean lineal intercept method [61], measuring at least 500 individual grains.

Two layers, as-deposited respectively annealed at 500 °C for 20 h, were selected for analysis by transmission electron microscopy (TEM). Each sample was cut to a small piece of ~1 × 10 mm². A protective silicon plate was mounted on top with an epoxy glue to form a sandwich, which was subsequently embedded in a copper tube. Thin slices cut from the tube (0.4 mm) were ground and polished to a disk with a thickness of ~0.1 mm, the center of which was thinned afterwards on a Gatan 656 dimple-grinder to a ~20 μm thick membrane. The membranes were etched to electron transparency by 3 keV Ar ion milling on a Gatan 691 Ion Polishing System. Conventional bright field images as well as selected area electron diffraction patterns were acquired using a Philips CM12 (100 kV, point to point resolution: 0.33 nm), a Philips CM30ST and a FEI Tecnai F30 FEG transmission electron microscope (300 keV, point to point resolution: ~0.2 nm).

3. Results and discussion

3.1. Phase composition and stress in ex-situ post-annealed YSZ films

Fig. 1 shows an overview of X-ray diffraction patterns for PLD-grown YSZ films, which were exposed to a 20 h isothermal post-annealing at different temperatures. The as-deposited layer and the one annealed at 200 °C exhibit exclusively sharp reflections of the sapphire substrate. A detailed view reveals an additional weak and broad 'halo' (FWHM ~5°) in the 2θ regions where reflections are expected for the cubic fluorite structure. Differently, distinct film-related peaks are observed for annealing temperatures ≥ 250 °C in addition to the substrate reflections. Their pattern matches the cubic fluorite-type phase (space group Fm3m, the ICDD powder reference is

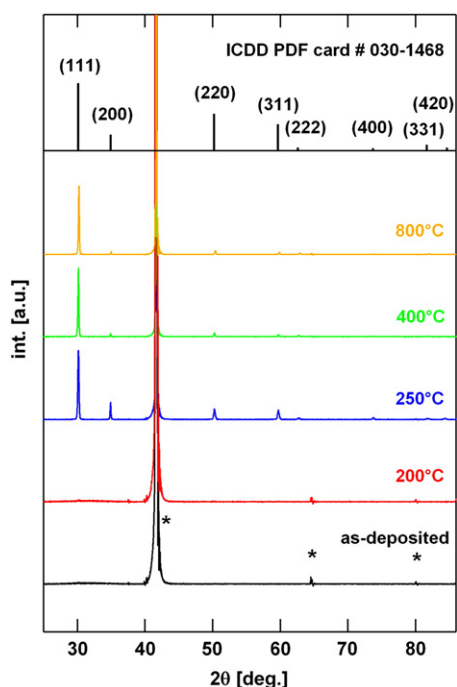


Fig. 1. X-ray diffraction patterns of 1.2 μm thick PLD-grown YSZ films, which were post-annealed ex-situ at different peak temperatures for an isothermal dwell time of 20 h. Intensities are normalized to the (111) reflection. Reflections of the sapphire substrate are marked with an asterisk. The individual patterns are offset and the dominant Al_2O_3 (0006) reflection at $2\theta = 41.685^\circ$ is cut for clarity. Miller indices, peak positions and intensities for an 8 mol% Y_2O_3 -doped ZrO_2 powder reference sample (ICDD powder diffraction database entry # 030-1468) with cubic fluorite structure are included for comparison.

included in Fig. 1 for comparison) commonly found for fully-stabilized zirconia [62] and reveals a preferential (111) orientation with respect to the surface normal of the sapphire substrate, which is particularly favored above 400 °C. The film diffractograms revealed no reflections due to impurities or secondary phases, proving that interfacial reactions of the YSZ films with the alumina substrate and cation interdiffusion are negligible up to temperatures of 1000 °C.

The absence of film-related distinct peaks, confirms the amorphous nature of the as-deposited YSZ layers, as found previously for PLD at ambient temperature [21,31,52]. The observed 'halo' reflects the near-range order in the amorphous state [63] that is retained up to an annealing temperature of 200 °C. The appearance of sharp reflections in addition to the substrate signals at higher temperatures indicates long-range ordering and marks the crystallization of the film. The observed preferential (111) orientation of the formed grains is consistent with the texture of as-deposited crystalline YSZ thin films grown by PLD at elevated substrate temperature [52]. The texture indicates comparatively low interfacial and surface energies of (111) oriented grains [37].

The X-ray diffraction patterns for temperatures ≥ 250 °C in Fig. 1 match unambiguously with the cubic fluorite-type phase of zirconia revealing e.g. no evidence for a splitting of the ($h00$) reflections to a doublet peak structure, which would be indicative of a tetragonal phase. However, the complexity of the Y_2O_3 – ZrO_2 phase diagram requires the complementary use of Raman spectroscopy as a sensitive probe for light elements such as oxygen for a reliable identification of the crystalline phase [64,65].

Fig. 2 presents Raman spectra of PLD-grown YSZ films annealed at different temperatures. The as-deposited film exhibits only a very weak and broad Raman signal ~ 550 – 600 cm^{-1} in addition to the sharp peak at 489 cm^{-1} as the single mode of the LaAlO_3 substrate in the investigated spectral range [66]. Differently, the film crystallized

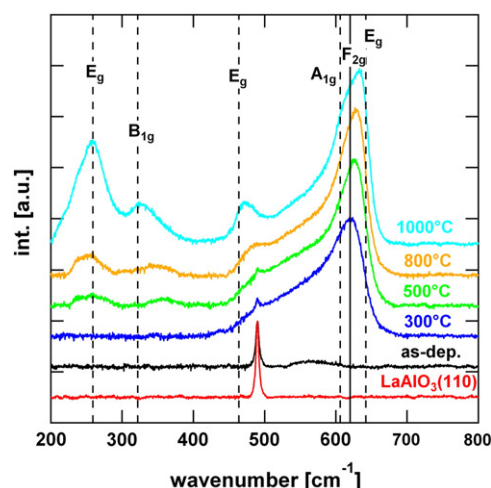


Fig. 2. Background corrected micro Raman spectra (λ : 632.8 nm) of as-deposited and annealed (different peak temperatures, 20 h isothermal dwell time) $\sim 1.2\text{ }\mu\text{m}$ thick YSZ films grown by PLD at room temperature. A spectrum of the uncoated LaAlO_3 (110) substrate is included as a reference. The individual spectra are offset for clarity. The vertical lines mark the positions of the Raman bands reported for a) tetragonal (dashed lines) and b) cubic (solid line) bulk YSZ [68,69].

at 300 °C reveals a strong asymmetric Raman signal with a maximum at 620 cm^{-1} and a pronounced low frequency shoulder. A systematic blue shift of this mode and the appearance of additional bands $\sim 257\text{ cm}^{-1}$, 325 – 370 cm^{-1} , 470 – 480 cm^{-1} are observed towards higher annealing temperatures (≥ 500 °C). Table 1 summarizes the observed Raman shifts and FWHM in comparison to reference data for microcrystalline YSZ powder samples of the cubic respectively tetragonal phase and provides assignments of the individual modes in accordance with the literature. The single peak at 620 cm^{-1} is due to the F_{2g} symmetric O–Zr–O stretching mode, characteristic for the cubic modification of zirconia [67,68], which proves the exclusive formation of this phase at low annealing temperatures (300 °C). The lower symmetry of tetragonal zirconia results in a larger number of Raman-active modes, i.e. an E_g stretching mode $\sim 259\text{ cm}^{-1}$, two coupled Zr–O bending and stretching modes at $\sim 322\text{ cm}^{-1}$ (B_{1g}) respectively $\sim 464\text{ cm}^{-1}$ (E_g), and the symmetric (A_{1g}) and asymmetric (E_g) O–Zr–O stretching modes at $\sim 606\text{ cm}^{-1}$ and $\sim 642\text{ cm}^{-1}$, respectively [68,69]. These peaks are observed, partly slightly shifted, for annealing temperatures ≥ 500 °C in addition to the F_{2g} mode and evidence thus the transition to a phase mixture of cubic and tetragonal zirconia. The systematic blue shift of the peak $\sim 620\text{ cm}^{-1}$ towards higher annealing temperature can be accounted for by the superposition of the F_{2g} band of the cubic phase (620 cm^{-1}) and the A_{1g} (606 cm^{-1}) and dominant E_g (642 cm^{-1}) bands of the tetragonal modification indicating an increasing fraction of the tetragonal phase. The latter may unambiguously be identified as the t'' metaphase by the total evidence of Raman spectra revealing tetragonal zirconia while the corresponding X-ray diffractograms show cubic symmetry [64,65].

As seen above, crystallization of the YSZ films at low to intermediate temperatures results in the exclusive (300 °C) or preferential (500–800 °C) formation of the cubic phase. A structural similarity between the cubic phase and the initial amorphous state has been suggested to explain analogous results for YSZ gels and films deposited by wet chemical techniques [28,70]. The transformation to more stable, but simultaneously more complex phases of lower symmetry seems to require a higher thermal activation. This behavior speaks in favor of a kinetically controlled transformation and contrasts the common finding of a transition to phases of higher symmetry with increasing temperature for thermodynamic control. The effect of the selection of the substrate on the film properties is supposed to be negligible as the latter

Table 1
Raman shifts, FWHM and assignment of the modes observed in the spectra of annealed YSZ thin films (Fig. 2) in comparison to reference data of sintered microcrystalline YSZ samples of the cubic respectively tetragonal phase and the LaAlO₃ substrate.

Material	$T_{20\text{ h}}$ [°C]	Raman shift [cm ⁻¹]	FWHM [cm ⁻¹]	Mode assignment
LaAlO ₃ (110)	–	489.9	4.5	E _g bending mode (LAO) [66]
μ-crystalline YSZ (cubic phase)	–	617.2	54.3	F _{2g} symmetric O–Zr–O stretching mode [68]
μ-crystalline YSZ (tetragonal t' phase)		256.5	30.3	E _g O _{II} –Zr–O _{II} stretching mode [68,69]
		318.2	29.8	B _{1g} coupled Zr–O bending and stretching mode [68,69]
		460.7	27.4	E _g coupled Zr–O bending and stretching mode [68,69]
		603.4	51.4	A _{1g} symmetric O–Zr–O stretching mode [68]
		640.0	23.8	E _g asymmetric O–Zr–O stretching mode [68]
YSZ film	as-dep.	489.9	4.8	E _g (LAO)
		568.5	50.5	O–Zr–O stretching (amorphous YSZ)
		490.2	5.0	E _g (LAO)
	300	620.0	78.0	F _{2g} (c-YSZ)
		257.0	42.6	E _g (t-YSZ)
		358.5	41.3	B _{1g} (t-YSZ)
	500	490.2	5.0	E _g (LAO)
		626.1	59.5	F _{2g} (c-YSZ) + A _{1g} and E _g (t-YSZ)
		252.6	40.4	E _g (t-YSZ)
	800	343.1	72.7	B _{1g} (t-YSZ)
		484.4	37.4	E _g (t-YSZ)
		628.8	52.8	F _{2g} (c-YSZ) + A _{1g} and E _g (t-YSZ)
	1000	257.3	49.7	E _g (t-YSZ)
		326.6	53.7	B _{1g} (t-YSZ)
		472.0	33.4	E _g (t-YSZ)
		632.9	55.1	F _{2g} (c-YSZ) + A _{1g} and E _g (t-YSZ)

are predominantly determined by the applied kinetically impeded PLD conditions that e.g. prevent substrate-induced oriented growth. Accordingly, Raman spectra of YSZ films grown by PLD on c-cut sapphire substrates and subsequently annealed analogously to the YSZ films grown on LaAlO₃ exhibited by tendency the same findings, however, the spectra were obscured by the superposition of film and substrate peaks.

The weak and broad Raman signal at 550–600 cm⁻¹ of the as-deposited YSZ layer can be attributed to O–Zr–O stretching vibrations in the structurally disordered amorphous state. An analogous red shift of the F_{2g} stretching mode was observed for amorphous versus crystalline CeO₂ thin films [15]. Generally, different factors such as phonon confinement, nonstoichiometry, defects and stress are discussed to affect the position, width and shape of Raman peaks [67,71,72]. In the case of the YSZ films the first two factors are negligible since the layers exhibited considerably large grains (>100 nm) and were stoichiometric within the detection limits, as discussed later, which limits the discussion to the effects of stress and defects.

Following Ortiz et al. [73] residual stresses can be classified to their active domain dimensions with i) macroscopic stress e.g. by mechanical or thermal treatments, ii) intergranular or interphase stress on the μm-level and iii) intragranular microstrain by lattice defects on an atomic level such as dislocations or stacking faults. Stresses of the category i) or ii) are known to affect the position of Raman peaks. For instance, Tanaka et al. [74] reported a linear dependence of the peak position of the asymmetric O–Zr–O stretching mode for tetragonal YSZ on macroscopic uniaxial stress. They find that compressive stress translates to a blue shift of the Raman peaks. Accordingly, the observed blue shift of the peak positions in the spectra of the PLD-grown YSZ films versus the microcrystalline reference data (Table 1), e.g. at 620 cm⁻¹ (film annealed at 300 °C) versus 617.2 cm⁻¹ (microcrystalline cubic YSZ) for the F_{2g} mode, suggests considerable compressive stress in the layers. This is supported by cubic lattice parameters, *a*, calculated from the peak positions in the film X-ray diffraction patterns, in the range of 5.12(2) to 5.13(2) Å, i.e. consistently smaller than the reference value of 5.139 Å for stress-free microcrystalline powder. Compressive stress may e.g. result from the mismatch of the thermal expansion coefficients between substrate and film, $\Delta\alpha \sim 6.5 \cdot 10^{-6} \text{ K}^{-1}$, upon cooling of the plasma-heated surface in the deposition process, from the peening effect by species with high kinetic energies impinging on the film surface during

film growth or from intergranular stress induced within the crystallization step. The Raman peak positions approach the values of the practically stress-free powder reference with increasing annealing temperature, shifting for instance from 358.5 cm⁻¹ (500 °C) to 343.1 cm⁻¹ (800 °C) and 326.6 cm⁻¹ (1000 °C) for the B_{1g} mode of the tetragonal phase with a reference value of 318.2 cm⁻¹ (Table 1). This evidence indicates that the compressive stress relaxes partially upon the heat treatment of the thin films.

Moreover, it has been shown for ceria thin films and nanocrystalline powders that asymmetric line profiles and peak broadening result from microstrain [15,75]. The FWHM of the F_{2g} mode was reported to increase with the lattice disorder from ~9 cm⁻¹ for microcrystalline CeO₂ powder, to ~15 cm⁻¹ for crystalline thin films and ~25 cm⁻¹ for amorphous layers [15]. These values are small compared to YSZ with e.g. a FWHM of 54.3 cm⁻¹ observed for the same mode in the case of a microcrystalline sample of the cubic structure (Table 1). However, unlike the situation for undoped metal oxides, the large FWHM and asymmetry of the Raman peaks in YSZ such as the low frequency shoulder of the band at ~620 cm⁻¹ are induced and dominated by the structural disorder associated with the high level of oxygen vacancy defects introduced to the ZrO₂ lattice by the yttria dopant [67,76]. An additional microstrain-related contribution to peak broadening can be expected for the PLD-grown YSZ films since they reveal larger FWHM values than the corresponding microcrystalline reference samples (Table 1), e.g. a maximum FWHM of 78 cm⁻¹ for the F_{2g} mode of the layer annealed at 300 °C.

A quantification of the microstrain present in the annealed films is possible by a detailed analysis of the angular variation of the peak width for the X-ray diffraction data. Correspondingly, Fig. 3a) displays representative Williamson–Hall plots for YSZ layers exposed to different annealing temperatures from which the grain size, *D*, and microstrain, ε , can be determined according to Eq. (7). Grain sizes derived from the y-axis intercept were consistently >100 nm, i.e. beyond the size limit for a reliable precise determination by XRD [60]. Consequently, the major source of peak broadening was found to be the microstrain, derived from the slope of the $\Delta(2\theta)_c \cdot \cos\theta$ versus $\sin\theta$ plots. Fig. 3b) shows that the microstrain decreases continuously with increasing annealing temperature as the lattice defects ‘heal’, similar to findings by Dura et al. [63] on mechanically alloyed YSZ powders. The absolute values of ε (~0.1–0.4%) are about one order of magnitude

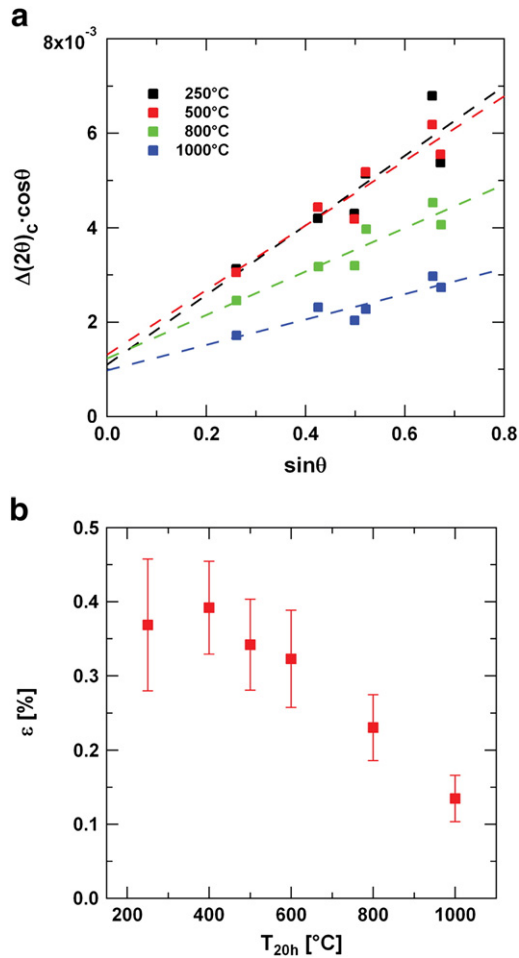


Fig. 3. a) Williamson–Hall plots for $\sim 1.2 \mu\text{m}$ thick PLD-grown, initially amorphous YSZ films annealed at different temperatures for 20 h. The microstrain, ε , shown in b) as a function of the annealing temperature is deduced from the slope of the linear regression fits in a).

smaller compared to thin films deposited by wet chemistry techniques such as spray pyrolysis [39], indicating the higher structural order obtained in the as-deposited amorphous layers by the solvent-free PLD technique.

The crystallization temperature of 200–250 °C as determined via XRD and Raman spectroscopy for the amorphous PLD-grown YSZ layers is remarkably low compared to the higher values of 400–500 °C, which have been reported for amorphous YSZ powders and gels prepared by co-precipitation or sol–gel processes [26–28,77] and thin films deposited by spray pyrolysis [70]. Similar to the results of this work, Kiguchi et al. [33] report a relatively low crystallization temperature of ~ 300 °C for amorphous 8 mol% yttria-doped zirconia layers deposited by PLD on Si substrates. The disparity between the crystallization temperatures of amorphous YSZ material prepared by PVD respectively non-vacuum methods is probably related to the fundamentally different energetic conditions of the deposition techniques. In the wet chemistry based techniques only the thermal energy of kT (on the order of 0.1 eV) is available for nucleation and growth processes during deposition, whereas highly energetic species (1–100 eV) are present in pulsed laser deposition even at low substrate temperatures due to the significant contributions of the kinetic energy and electronic excitation [78]. Amorphous structures obtained by low temperature PLD attain probably a closer structural relation to the equilibrium crystalline state compared to thermal deposition techniques, which results in films with lower levels of microstrain as discussed above. Subcritical nuclei requiring only a

small thermal activation for crystallization to a well ordered lattice upon post-annealing can be expected in this case. On the other hand, solvent residuals, which are omnipresent in the metal oxide films deposited by a wet chemistry approach, may inhibit the crystallization process [79]. Rupp et al. [15] reported for instance that the choice of organic glycol lengths and their boiling points affects the packing density, near-ordering and the crystallization temperature of amorphous metal oxide films prepared by spray pyrolysis.

3.2. Crystallization kinetics of YSZ thin films by in-situ hot-stage XRD experiments

The isothermal crystallization kinetics of the YSZ thin films were investigated using the in-situ hot-stage XRD technique for layer thicknesses of 200 nm and $1.2 \mu\text{m}$ in the temperature range of 200–400 °C. Fig. 4 presents examples for the temporal evolution of the (111) reflection recorded during isothermal dwells at annealing temperatures of 275 °C and 325 °C for 200 nm thick layers. In the case of the film annealed at 275 °C, a weak signal starts to appear after ~ 45 min, indicating the onset of the crystallization process, which proceeds continuously until after ~ 3 h a constant peak intensity is reached, marking the completion of the phase transformation. At the elevated temperature of 325 °C the crystallization starts practically instantaneously and advances on a minute time scale as evidenced by the increasing peak intensities. In this case, the process is accomplished after 5–10 min. Remarkably, the FWHM does not change

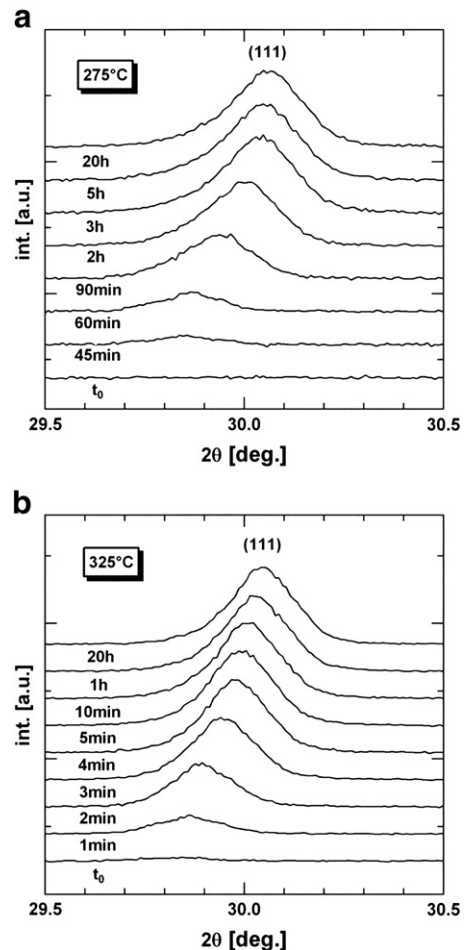


Fig. 4. In-situ X-ray diffractograms of initially amorphous, as-deposited ~ 200 nm thin YSZ layers at annealing temperatures of 275 °C and 325 °C showing the temporal evolution of the (111) reflection. The individual diffraction patterns are offset for clarity.

significantly during the transformation process indicating a fast and abrupt formation of large grains with dimensions >100 nm, i.e. the intermediate nanocrystalline state, which would result in pronounced XRD peak broadening (compare Eq. (7)), is short lived and not stable. Analogously, Nichtova et al. [80] report about a rapid formation of large grains and a negligible density of nm-sized crystallites during the crystallization of TiO_2 films prepared by magnetron sputtering.

The crystallized volume fraction, $x(t)$, can be quantified from the integrated peak areas of the transient diffractograms according to Eq. (8). The extracted degree of crystallinity is displayed in Fig. 5 on a logarithmic time scale for all investigated films and annealing conditions. In accordance with the ex-situ annealing experiments in air, no crystallization is observed within the in-situ XRD experiments in vacuum at temperatures below 250°C up to 20 h dwell time. At temperatures $\geq 350^\circ\text{C}$ the phase transformation is completed already during the heating ramp. In the temperature range of 250 – 325°C the curves reveal a characteristic sigmoidal shape. At the lower temperatures the phase transformation starts only after a thickness-independent induction period, which exhibits a strong temperature dependency increasing from ~ 5 min (300°C) over ~ 25 min (275°C) to ~ 3 h (250°C), whereas at $T \geq 325^\circ\text{C}$ the process starts instantaneously. The induction period is related to the nucleation process [81], which is characterized by a change of Gibbs free energy, ΔG , given by [33]

$$\Delta G = \left[\frac{4}{3}\pi r^3 \cdot \Delta G_c + 4\pi r^2 \cdot \gamma + \frac{4}{3}\pi r^3 \cdot \varepsilon \right] \cdot S(\theta_c) \quad (9)$$

where

$$S(\theta_c) = \frac{(2 + \cos\theta_c)(1 - \cos\theta_c)^2}{4} \quad (10)$$

with θ_c as the contact angle and r as the radius of a nucleus. The chemical potential difference between the amorphous and crystalline phase ($\Delta G_c < 0$) acts as the driving force of the phase transformation, while the surface energy, $\gamma > 0$, imposed by the formation of a new internal interface and the elastic strain energy, $\varepsilon > 0$, caused by the volume change upon crystallization represent retarding terms in Eq. (9). As a result, only nuclei above a critical size are thermody-

namically stable and grow spontaneously. The formation of critical nuclei is a thermally activated process with an activation energy, ΔG^* , of [33]

$$\Delta G^* = \frac{16\pi\gamma^3}{3(\Delta G_c - \varepsilon)^2} \cdot S(\theta_c). \quad (11)$$

Hence, the observed induction period can be attributed to the formation of critical nuclei from subcritical seeds present in the original material, which is kinetically impeded below 325°C .

Fig. 5 reveals moreover a systematically slower phase transformation for the thicker films. This behavior is expected for (preferential) heterogeneous nucleation at the interface(s) as the volume fraction of the interfacial region decreases with increasing total film thickness. Heterogeneous nucleation is energetically favored by the geometrical term, $S(\theta_c)$, which lowers the activation barrier for the formation of critical nuclei in Eq. (11) for contact angles $< 180^\circ$ (homogeneous nucleation: $\theta_c = 180^\circ$). Additionally, the density of defects acting as nucleation sites is commonly higher at interfaces than in the bulk of a phase, which promotes interfacial nucleation in thin film systems. On the contrary, no thickness dependence of the degree of phase transformation would be expected in the case of homogeneous nucleation since the process could start within the whole volume of the initial amorphous film [82].

According to Eq. (1) the linear behavior of the experimental phase transformation data in plots of $\ln[-\ln(1-x)]$ versus $\ln t$ (Fig. 6) verifies that the crystallization of the amorphous PLD-grown YSZ films proceeds via nucleation and grain growth. The crystallization kinetics can be described by the JMAK model with a time-independent rate constant. The values of the rate constant, k , and the Avrami exponent, n , calculated from the y-axis intercept respectively the slope of the linear regression fits in Fig. 6 are summarized in Table 2.

The Avrami exponent is close to $n=3$ (200 nm thick films) respectively slightly lower, $n \sim 2.7$ ($1.2\ \mu\text{m}$ thick films), for annealing temperatures in the range of 250 – 300°C . Significantly lower values of $n \sim 1.8$ are obtained for annealing at a higher temperature of 325°C . The absolute values of the Avrami exponent are frequently interpreted with respect to the crystallization mechanism, in terms of the dimensionality of the transformation or the nature of a diffusion-controlled process. For instance a three dimensional (hemi)spherical growth is expected to yield $n=4$ in the case of continuous nucleation respectively $n=3$ in the case of initial seeding [27,83]. However, in the case of thin films, a simple mechanistic interpretation is not possible without further evidence e.g. from TEM studies as finite size

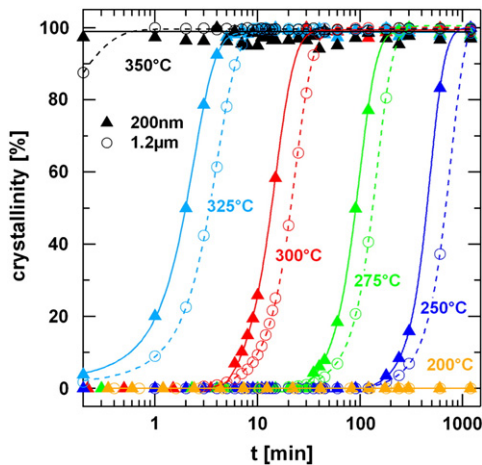


Fig. 5. Degree of crystallinity calculated from the integrated intensity of the (111) reflection of the in-situ XRD patterns as a function of dwell time at different peak temperatures for initially amorphous, as-deposited YSZ films of 200 nm and $1.2\ \mu\text{m}$ thickness.

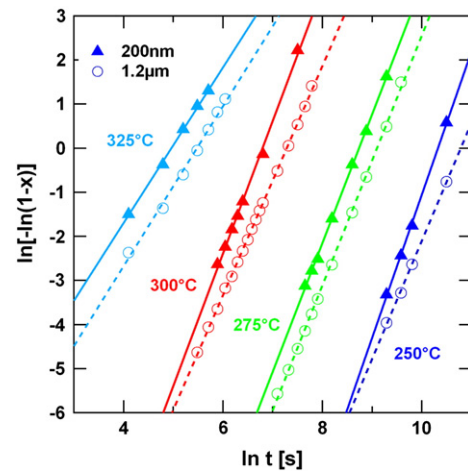


Fig. 6. JMAK plots and linear least square fits for the kinetic crystallization data obtained at different isothermal dwell temperatures for PLD-grown initially amorphous YSZ layers of 200 nm and $1.2\ \mu\text{m}$ thickness.

Table 2

Avrami exponents, n , and rate constants, k , derived from the least square linear fits in the JMAK plot (Fig. 6).

T [°C]	200 ± 10 nm thick films		1200 ± 30 nm thick films	
	n	k [s ^{−n]}	n	k [s ^{−n]}
250	3.25	$2.7 \cdot 10^{-15}$	2.68	$2.9 \cdot 10^{-13}$
275	2.92	$8.4 \cdot 10^{-12}$	2.83	$6.4 \cdot 10^{-12}$
300	3.00	$1.4 \cdot 10^{-9}$	2.60	$6.1 \cdot 10^{-9}$
325	1.76	$1.6 \cdot 10^{-4}$	1.81	$4.9 \cdot 10^{-5}$

effects lead to deviations from the ideal model. Weinberg et al. [84] demonstrated that finite size effects and non-uniform nucleation generally cause a decreasing transformation rate and a reduction of the Avrami exponent. Nevertheless, relative changes of n may serve as an indicator to alterations in the crystallization mechanism. Thus, the pronounced change of the Avrami exponent between 325 °C and 300 °C (compare Table 2) is attributed to a transition from initial, instantaneous nucleation for $T > 300$ °C to continuous nucleation at lower temperatures (250–300 °C) for which a change by $\Delta n = +1$, as experimentally observed, would be anticipated theoretically. Such behavior would be rational as the fraction of nuclei with sufficient energy to pass the activation barrier and reach the critical size for ongoing spontaneous growth increases with the temperature until all available seeds are activated practically instantaneously. This interpretation is supported by the previously discussed alteration of the induction behavior (Fig. 5).

The rate constant k increases systematically with the temperature (Table 2). The plot of $\ln k$ versus T^{-1} in Fig. 7, which includes only data up to 300 °C due to the observed change of mechanism at higher temperatures, reveals an Arrhenius-type behavior according to Eq. (2). From the slope of the least square linear fits activation energies of 6.8 ± 0.7 eV (200 nm thick films) respectively 5.1 ± 1.3 eV (1.2 μm thick films), which are indicative of a strong thermal activation, are determined. Activation energies in the range of a few eV are characteristic for bulk diffusion controlled processes, whereas surface or grain boundary diffusion control typically yields lower values in the range of 0.1–1 eV. In the case of yttria-stabilized zirconia oxygen vacancies are present in a high concentration, imparting the mobility of anions. It is therefore reasonable to assume that the diffusion of the cations represents the rate determining step. Chien and Heuer [85] report an activation energy of 5.3 ± 0.1 eV for the Zr diffusion in single crystalline YSZ via point defects. This value agrees

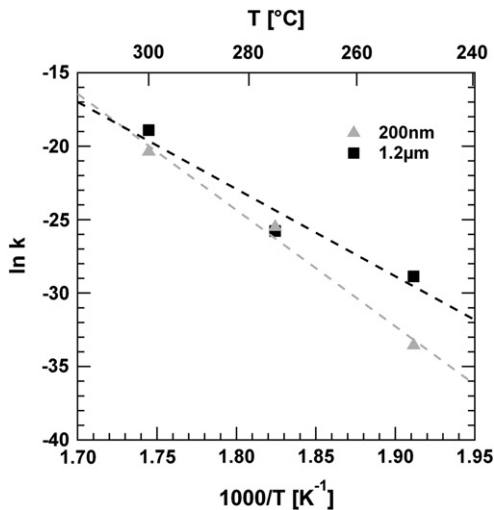


Fig. 7. Temperature dependence of the rate constant k for the crystallization of PLD-grown YSZ films at $T \leq 300$ °C in an Arrhenius plot.

well with the data for the PLD-grown YSZ layers supporting the suggested mechanism of a cation bulk diffusion controlled phase transformation. Lower activation energies in the range of 2.4–3.5 eV are commonly observed for the crystallization of YSZ powders and gels [27,28], which illustrates the influence of the sample preparation on solid state defect chemistry. The situation in a PLD-grown YSZ film is certainly closer to a single crystal than to gels and powders derived by wet chemistry techniques, which contain solvent residuals and a higher degree of structural disorder, as the following comparison of the packing densities confirms.

The peak maxima of the in-situ diffractograms shift continuously to larger Bragg angles with progressing annealing time, as shown in Fig. 4, which is indicative of a densification. The shift of the peak maxima in the X-ray diffractograms may also partly be due to the relaxation of compressive in-plane stress, which might reduce the out-of-plane lattice parameter without affecting the total cell volume. This effect is neglected in this simplified approach based entirely on the measurement of the out-of-plane lattice parameter, which is assumed to represent exactly the in-plane lattice parameters in view of the cubic symmetry. A quantitative determination of the crystallographic densities from the XRD peak positions by Eq. (5) moreover requires knowledge of the film stoichiometry, which was determined by a combination of Rutherford backscattering (RBS) and particle induced X-ray emission (PIXE) as described elsewhere [86]. No significant changes of the composition were found within the investigated range of annealing conditions. The mean film stoichiometry of $\text{Zr}_{0.845 \pm 0.004} \text{Y}_{0.155 \pm 0.004} \text{O}_{1.92 \pm 0.04}$ was utilized for quantification of the crystallographic density, neglecting the detected content of ~1 at% Hf (referred to the sum of cations) for the sake of comparability to literature density data, which commonly do not account for the ubiquitous hafnia impurities.

The temporal evolution of the crystallographic density is plotted in Fig. 8 on a logarithmic time scale for all investigated thicknesses and annealing temperatures. It has to be considered that the crystallographic density relates exclusively to the crystalline fraction of the film, i.e. the real film density might be significantly lower in the biphasic region due to the presence of the amorphous phase. A major, sharp increase of the crystallographic density is observed in the initial phase attributed to the crystallization in each case, except for 350 °C, where the process is almost accomplished already during the heating ramp. A slow, steady further increase of the crystallographic density is

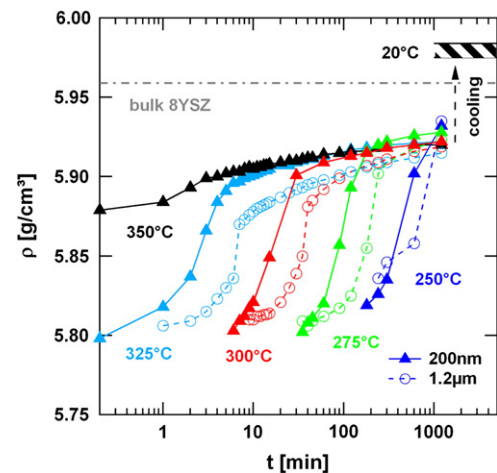


Fig. 8. Crystallographic density as a function of dwell time at different peak temperatures for initially amorphous, as-deposited YSZ films of 200 nm and 1.2 μm thickness. The vertical arrow illustrates the change of the density upon cooling to room temperature due to thermal contraction, which yields density values within the range marked by the hatched region. The horizontal dashed line indicates the density of cubic 8YSZ (20 °C) calculated from the powder reference pattern (ICDD PDF card # 00-030-1468), which is included as a reference.

found after the completion of the crystallization process. This can be rationalized in terms of the ordering of the crystal lattice, i.e. the reduction of the microstrain, which advances with increasing temperature (compare Fig. 3), but also progressing dwell time. The overall apparent change of the crystallographic density after 20 h annealing time translates to a mean volumetric contraction of the film by $2.0 \pm 0.2\%$. This value is rather low compared to volumetric changes of $\sim 15\%$ reported for the crystallization of wet-chemistry based metal oxide thin films [16] and can be attributed to the enhanced near range order and the absence of solvent residuals for the amorphous PLD-grown films. A small volumetric change is important from an application perspective as it minimizes the associated stresses that may cause rupture of the film upon crystallization.

The mean linear thermal expansion coefficient, α , of the YSZ films can be deduced from the change of the crystallographic density upon cooling to room temperature, indicated by the dashed vertical arrow in Fig. 8, yielding a value of $\alpha = (11.1 \pm 0.7) \cdot 10^{-6} \text{ K}^{-1}$, which is close to the reference value of $10.5 \cdot 10^{-6} \text{ K}^{-1}$ for the bulk material [87]. Crystallographic densities at ambient temperature, which are above the reference value of 5.96 g/cm^3 for microcrystalline 8 mol% Y_2O_3 -stabilized zirconia powder relate to residual compressive stress in the films as discussed above. The crystallographic density of the as-deposited amorphous YSZ films can be estimated to be $5.86 \pm 0.1 \text{ g/cm}^3$ taking into account the thermal contraction. This value is only slightly smaller than the density of an 8 mol% Y_2O_3 -doped zirconia single crystal (5.99 g/cm^3) [88] confirming the high packing density in the amorphous PLD-grown YSZ layers. Packing densities considerably lower than the theoretical density are typically reported for amorphous wet chemistry based metal oxide thin films [15].

3.3. Grain growth of YSZ thin films studied by electron microscopy

Two 200 nm thick YSZ film samples, i) as-deposited and ii) annealed at 500°C (20 h) were selected for investigation by transmission electron microscopy to visualize the microstructural changes upon heat treatment, aiming at a better understanding of the crystallization process.

Fig. 9a) shows a bright-field TEM image of an as-deposited PLD-grown YSZ layer, which was obtained at minimum beam irradiance with a defocused electron beam. The film is dense and appears mostly homogeneous; however, a weak contrast is visible at some locations. The corresponding diffractogram (inset in Fig. 9a) reveals that the main part of the intensity is allocated to diffuse rings, although they are interspersed with a small number of singular spots. These observations indicate that the film is predominantly amorphous, but a few small crystallites with dimensions of 5–10 nm are present.

Fig. 9b) illustrates the effect of a short exposure of the film to the electron beam focused on a spot with $\sim 300 \text{ nm}$ diameter and centered on the depicted part of the layer. Grains with average dimensions of $\sim 20 \text{ nm}$ are clearly visible throughout the film as dark regions, while the corresponding diffractogram (inset in Fig. 9b) reveals a significant increase in the number and intensity of diffraction spots with a weaker diffuse background. These observations clearly indicate an electron beam induced crystallization and confirm the high sensitivity of the as-deposited PLD-grown YSZ layers, which require only a weak stimulus to initiate the phase transition. This suggests that the initial layer is purely amorphous and the small crystallites detected in Fig. 9a) originate from the low electron beam irradiance required for imaging. Electron beam induced crystallization of amorphous metal oxide films is well documented in the literature. Shimizu et al. [89] observed for instance that amorphous anodic alumina barrier layers, which are thermally stable up to 700°C , crystallize under electron beam irradiance in a TEM at room temperature. Roddatis et al. [90] report on the high sensitivity of thin zirconia films towards beam induced crystallization, which proceeds within 1 min at room temper-

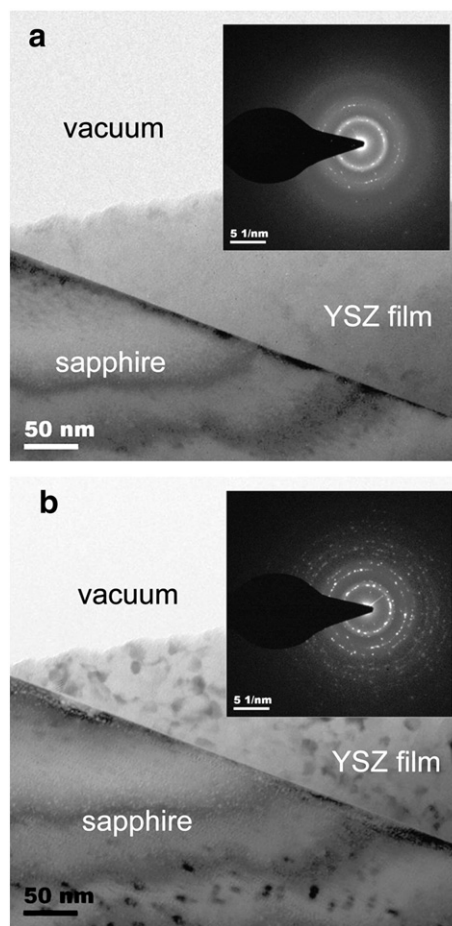


Fig. 9. Bright field transmission electron micrographs of a $\sim 200 \text{ nm}$ thick YSZ layer grown by PLD at room temperature: a) as-deposited layer; image taken with a strongly defocused electron beam at minimum irradiance and without previous exposure of the site, b) as-deposited layer after focusing the electron beam to a diameter of $\sim 300 \text{ nm}$ on the film. The insets represent the corresponding electron diffractograms.

ature and only somewhat slower even at 4.2 K , using 200 keV and 400 keV electrons.

Fig. 9b) shows that the formed crystallites are dispersed randomly across the film indicating homogeneous nucleation while the in-situ XRD data suggested a preferential nucleation for the thermally induced phase transformation. Electron beam induced crystallization is likely to differ significantly from thermal activation since it is not a simple heating effect, but is dominated by the damage imparted by knock-on collisions [91,92]. These may actively create defects as nucleation sites in the irradiated area, whereas thermal crystallization relies on the present defects originating from the previous sample preparation steps. As observed within this work, electron beam irradiance typically induces the formation of comparatively small, randomly oriented polycrystals [90–92].

The sensitivity of the PLD-grown YSZ layers to electron beam induced crystallization even under 'soft' imaging conditions prevents the application of TEM to obtain reliable additional mechanistic insights to the thermal crystallization process for fully or partially amorphous films. On the other hand, the investigation of annealed, completely crystallized layers is unproblematic.

Fig. 10 depicts a TEM bright field image of an initially amorphous YSZ film, which was crystallized at 500°C for 20 h in air prior to imaging. The film exhibits large equiaxed grains with dimensions on the order of the film thickness and shapes that suggest a predominantly isotropic 3D growth mode. This would be compatible with the observed Avrami exponents if the depression of n by finite size effects

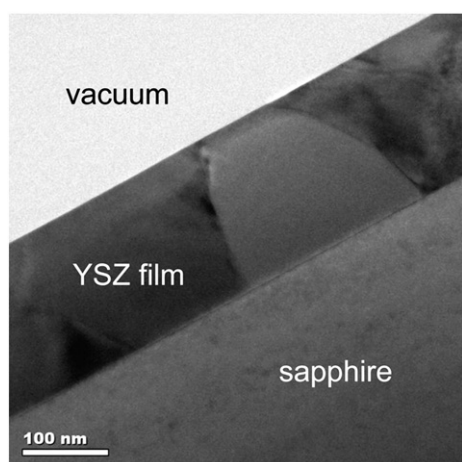


Fig. 10. Bright field transmission electron micrograph of a ~200 nm thick initially amorphous YSZ layer grown by PLD at room temperature and subsequently annealed at 500 °C (20 h) in air.

is considered. Many grains extend across the entire film thickness and are separated by distinct boundaries. The layer is dense and without any discernible pores. There are no indications for amorphous residuals, i.e. a fully crystalline state is attained in the YSZ layers by annealing at moderate temperatures. The grain morphology suggests

a heterogeneous nucleation process confirming the evaluation of the in-situ XRD data. Heterogeneous nucleation appears possible at both film interfaces. Kiguchi et al. [33] directly observed the nucleation in nanometric amorphous YSZ layers by in-situ TEM and located the onset of the thermal phase transformation close to the film surface. However, this is not related to an energetically advantageous situation inherent to the film/air interface, but a defect-rich surface layer that is formed during TEM sample preparation.

The top view SEM image of a YSZ film annealed at 1000 °C in Fig. 11a) confirms that large faceted grains are formed rapidly, i.e. within the crystallization process (<1 min duration at 1000 °C), which is in agreement with the Williamson–Hall analysis. The broad grain size distribution can be approximated by a logarithmic normal function. It shifts only slightly towards larger grain sizes with prolonged annealing time, e.g. from a mean grain size of 230 nm after 1 min (Fig. 11a) to 264 nm after 20 h (Fig. 11b). This shows that thermal grain coarsening is negligible once the crystallization process is completed, even at the upper limit of the investigated temperature range.

The observed behavior differs clearly from classical curvature-driven grain growth according to Eq. (3), which is commonly observed for bulk polycrystalline metals and ceramics [38]. The stagnation of normal grain growth of the YSZ thin films can be attributed to the specimen thickness effect by grain boundary grooving, which results in close to logarithmic normal grain size distributions [37,93]. An et al. [48] presented a three stage model of the grain size evolution in thin films based on Monte Carlo simulations taking into account the thickness effect. In stage 1 normal grain growth proceeds unimpeded as the average grain size is

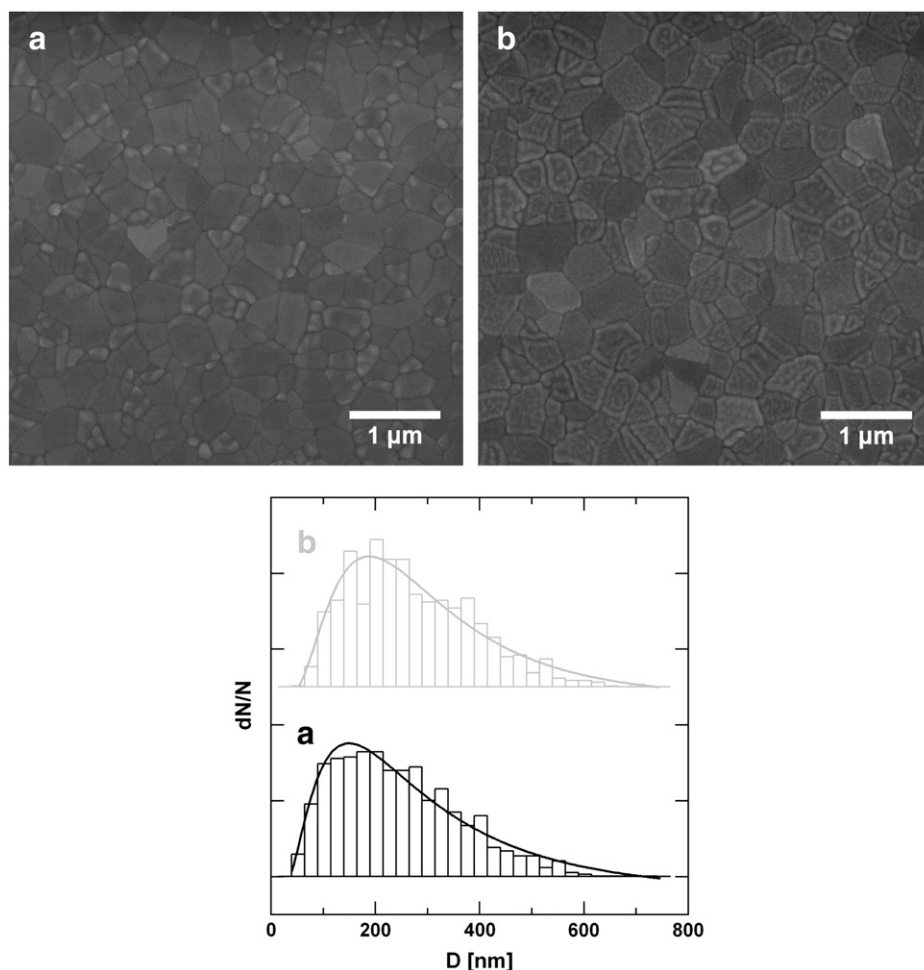


Fig. 11. SEM top view images of ~200 nm thick initially amorphous PLD-grown YSZ layers annealed at 1000 °C for a) 1 min and b) 20 h and corresponding grain size distributions (bottom). The solid lines represent least square fits to a logarithmic normal function.

well below the film thickness. Grain growth slows down with the formation of columnar grains that extend through the entire film and intersect the surface (stage 2). In stage 3 all grains extend through the film and growth almost stops except for the straightening of grain boundaries and the consumption of small grains by adjacent larger grains via Ostwald ripening. In the case of the PLD-grown YSZ films, large grains with dimensions of the film thickness are formed rapidly during the crystallization without a stabilization of intermediate nanocrystalline states, i.e. stage 2 is reached. The observed minor changes of the grain size distribution after completion of the phase transformation relate to the processes characteristic to stage 3.

This is again very different to the self-limited grain growth yielding metastable nanocrystalline microstructures with grain dimensions well below the film thickness, which was reported for the heat treatment of initially amorphous metal oxide films prepared by precipitation based methods such as spray pyrolysis [16,39,70] or spin-coating [50,94]. The inhibition of grain coarsening has been attributed to a stabilization of nanocrystallites by a grain-size dependent solute drag [43,50], elastic strain in amorphous phase residuals and to carbon impurities detected up to 1000 °C [16,51]. The comparison to this work suggests in particular that the non-equilibrium deposition conditions that favor atomic scale ordering and the absence of solvent impurities result in a lower density of nucleation sites incorporated by vacuum deposition processes. This promotes the growth of larger grains as observed for the PLD-grown YSZ films.

3.4. Microstructures of YSZ thin films prepared by pulsed laser deposition

Thermal post-annealing, as discussed above, extends the array of YSZ film microstructures that are accessible by PLD as Fig. 12 illustrates. As reported previously, dense YSZ films can be grown by PLD in an oxygen background atmosphere below a threshold pressure of 2.5 Pa [52,53]. Isotropic amorphous layers result at ambient temperature whereas polycrystalline coatings can be obtained directly at substrate temperatures ≥ 400 °C. For a growth temperature of 600 °C the latter consist of densely packed vertically aligned nanocolumnar grains that extend across the entire film thickness. This corresponds to a zone 2 type structure in Thornton's microstructural model as expected for a reduced temperature T/T_m of ~ 0.3 [95]. The lateral grain dimensions can be adjusted by the deposition pressure within a range of 10–100 nm.

The initially amorphous layers can be crystallized by thermal annealing, passing a transient biphasic state, to yield fully crystalline microstructures of equiaxed coarse grains with dimensions on the order of the film thickness, which differ significantly from the nanocolumnar structures. The considerably lower number density of grain boundaries per volume unit in the coarse grained microstructure affects the films' physical properties in a favorable fashion for solid electrolyte purposes. In particular, the electrical resistivity is lowered due to the blocking nature of grain boundaries in YSZ [96,97], while the resistance to chemical degradation by interdiffusion, which occurs preferentially along the grain boundaries, increases.

Furthermore, the extraordinary low crystallization temperature of 200–250 °C is important from an application perspective [1]. Accordingly, a two step PLD-based 'soft' processing route of crystalline YSZ membranes for Si wafer supported miniaturized electroceramic

devices such as solid oxide fuel cells [98] or gas sensors [56] can be envisioned. In the first step an amorphous YSZ layer would be applied to a pre-structured Si substrate by PLD at room temperature. Subsequently the YSZ layer would be crystallized by post-annealing e.g. at 250 °C. The moderate processing temperature, the observed small volume contraction upon crystallization, and the remarkable stability of the resulting crystalline microstructure versus grain growth minimize thermally induced degradation reactions respectively thermal and elastic stresses, which may cause failure of the thin film heterostructures [99].

4. Conclusions

The activation of the crystallization process in amorphous PLD-grown YSZ thin films requires only a weak stimulus. The exposure to an energetic electron beam induces the formation of randomly dispersed ~ 20 nm sized crystallites even at low doses and ambient temperature. Thermal post-annealing initiates the phase transformation at temperatures above an exceptionally low threshold of 200–250 °C compared to crystallization temperatures typically > 400 °C for YSZ gels, powders or films prepared by precipitation-based techniques. At low temperatures (< 500 °C) the cubic fluorite-type zirconia modification evolves whereas higher annealing temperatures favor the formation of the t'' phase.

The crystallization of the YSZ films, which is associated with a volume contraction of $\sim 2\%$, proceeds on a seconds to hours time scale in the investigated temperature range (200–1000 °C) and is completed after a maximum of 20 h. The isothermal crystallization kinetics can be described quantitatively within the framework of the JMAK model. The experimental evidence indicates a 3D isotropic grain growth with preferential heterogeneous nucleation and an activation energy of 5.1–6.8 eV characteristic for bulk cation diffusion control. A mechanistic change from continuous nucleation with a temperature dependent induction period for the formation of critical nuclei (250–300 °C) to initial seeding ($T \geq 325$ °C) is observed. Large equiaxed grains with dimensions > 100 nm are formed rapidly and the density of nm-sized crystals remains negligible during the phase transformation in contrast to the stabilization of nanocrystalline microstructures upon crystallization of amorphous metal oxide thin films derived by wet chemical deposition techniques. Normal grain growth of the PLD-grown YSZ films stagnates once the average grain size approaches the film thickness upon completion of the crystallization process due to the pinning of grain boundaries by surface grooves. The resulting fully crystalline microstructures are remarkably stable versus thermal grain coarsening. The enhanced grain growth and the significantly lower crystallization temperature of the amorphous YSZ films grown by PLD versus wet chemistry deposition techniques is due to the absence of inhibiting solvent impurities. Secondly, the non-equilibrium growth conditions during PLD promote an enhanced near range order in the as-deposited state, indicated by low microstrain values and the high density of 5.86 ± 0.1 g/cm³ for the amorphous films, which is close to the value of 5.99 g/cm³ for a single crystal. This yields a lower density of defects that act as nucleation sites.

The extraordinary low crystallization temperature for the amorphous PLD-grown YSZ layers and the small volume contraction

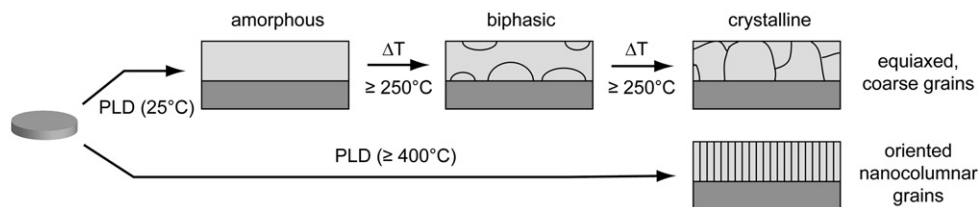


Fig. 12. Scheme illustrating the different YSZ layer microstructures accessible by a variation of the PLD parameters and post-annealing.

associated with the phase transformation are attractive for a ‘soft’ processing of solid electrolyte membranes for integration in Si supported miniaturized ceramic fuel cells or gas sensors. The microstructure consisting of coarse equiaxed grains obtained by post-annealing differs from the nanocolumnar structures resulting from the direct growth of crystalline layers by PLD at elevated temperatures. The corresponding reduction of the number density of grain boundaries, which exhibit a high specific resistance, can be foreseen to minimize the ohmic losses in solid electrolyte applications.

Acknowledgements

The project is part of the program ‘Nanocrystalline ceramic thin films without sintering’ (NANCER) funded by the Competence Center of Material Science and Technologies (CCMX) of the ETH board, Switzerland.

References

- [1] N. Settner, R. Waser, *Acta Mater.* 48 (2000) 151–178.
- [2] P.R. Willmott, *Prog. Surf. Sci.* 76 (2004) 163–217.
- [3] A.A. Voievodin, J.G. Jones, J.S. Zabinski, J. Vac. Sci. Technol. A 19 (2001) 1320–1324.
- [4] S. Yata, Y. Nakashima, T. Kobayashi, *Thin Solid Films* 445 (2003) 259–262.
- [5] S. Sriram, M. Bhaskaran, D.R.G. Mitchell, A. Mitchell, *Cryst. Growth Des.* 10 (2010) 761–764.
- [6] J. Will, A. Mitterdorfer, C. Kleinlogel, D. Perednis, L.J. Gauckler, *Solid State Ionics* 131 (2000) 79–96.
- [7] K.P. Biju, M.K. Jain, *Thin Solid Films* 516 (2008) 2175–2180.
- [8] D.C. Paine, T. Whitson, D. Janiac, R. Beresford, C.O. Yang, B. Lewis, *J. Appl. Phys.* 85 (1999) 8445–8450.
- [9] R. Rujkorakarn, J.R. Sites, J. Vac. Sci. Technol. A 4 (1986) 568–571.
- [10] J.L.M. Rupp, L.J. Gauckler, *Solid State Ionics* 177 (2006) 2513–2518.
- [11] A. Bhaskar, T.H. Chang, H.Y. Chang, S.Y. Cheng, *Thin Solid Films* 515 (2007) 2891–2896.
- [12] S.Y. Chen, I.W. Chen, *J. Am. Ceram. Soc.* 81 (1998) 97–105.
- [13] M. Es-Souni, A. Piorra, *Mater. Res. Bull.* 36 (2001) 2563–2575.
- [14] H. Hu, C.J. Peng, S.B. Krupanidhi, *Thin Solid Films* 223 (1993) 327–333.
- [15] J.L.M. Rupp, B. Scherrer, L. Gauckler, *Phys. Chem. Chem. Phys.* (2010), doi:10.1039/b920971a.
- [16] J.L.M. Rupp, B. Scherrer, A.S. Harvey, L.J. Gauckler, *Adv. Funct. Mater.* 19 (2009) 2790–2799.
- [17] C.C. Chen, M.M. Nasrallah, H.U. Anderson, *Solid State Ionics* 70 (1994) 101–108.
- [18] M.S.R. Rao, C.P. D’souza, P.R. Apte, R. Pinto, L.C. Gupta, S. Srinivas, A.K. Bhatnagar, *J. Appl. Phys.* 79 (1996) 940–946.
- [19] A.P. Caricato, A. Di Cristoforo, M. Fernandez, G. Leggieri, A. Luches, G. Majni, M. Martino, P. Mengucci, *Appl. Surf. Sci.* 208 (2003) 615–619.
- [20] J.H. Joo, G.M. Choi, *Solid State Ionics* 177 (2006) 1053–1057.
- [21] J. Zhu, Z.G. Liu, *Mater. Lett.* 57 (2003) 4297–4301.
- [22] Y.Z. Jiang, H.Z. Song, J.F. Gao, G.Y. Meng, *J. Electrochem. Soc.* 152 (2005) C498–C503.
- [23] D. Perednis, O. Wilhelm, S.E. Pratsinis, L.J. Gauckler, *Thin Solid Films* 474 (2005) 84–95.
- [24] A. Aronne, A. Marotta, P. Pernice, M. Catauro, *Thermochim. Acta* 275 (1996) 75–82.
- [25] D.Y. Chen, E. Jordan, M. Gell, *J. Mater. Sci.* 42 (2007) 5576–5580.
- [26] A. Ghosh, D.D. Upadhyaya, R. Prasad, *J. Am. Ceram. Soc.* 85 (2002) 2399–2403.
- [27] C.W. Kuo, Y.H. Lee, I.M. Hung, M.C. Wang, S.B. Wen, K.Z. Fung, C.J. Shih, *J. Alloy Compd.* 453 (2008) 470–475.
- [28] S. Ramanathan, R.V. Muraliedharan, S.K. Roy, P.K.K. Nayar, *J. Am. Ceram. Soc.* 78 (1995) 429–432.
- [29] S. Ramanathan, N.C. Soni, R. Prasad, *J. Mater. Sci. Lett.* 12 (1993) 122–124.
- [30] C.L. Ong, J. Wang, S.C. Ng, L.M. Gan, *J. Am. Ceram. Soc.* 81 (1998) 2624–2628.
- [31] A.P. Caricato, G. Barucca, A. Di Cristoforo, G. Leggieri, A. Luches, G. Majni, M. Martino, P. Mengucci, *Appl. Surf. Sci.* 248 (2005) 270–275.
- [32] P. Mengucci, G. Barucca, A.P. Caricato, A. Di Cristoforo, G. Leggieri, A. Luches, G. Majni, *Thin Solid Films* 478 (2005) 125–131.
- [33] T. Kiguchi, N. Wakiya, K. Shinozaki, N. Mizutani, *J. Mater. Res.* 20 (2005) 1878–1887.
- [34] M. Avrami, *J. Chem. Phys.* 7 (1939) 1103–1112.
- [35] M. Avrami, *J. Chem. Phys.* 9 (1941) 177–184.
- [36] W.A. Johnson, R.F. Mehl, *T. Am. I. Min. Met. Eng.* 135 (1939) 416–442.
- [37] C.V. Thompson, *Annu. Rev. Mater. Sci.* 20 (1990) 245–268.
- [38] J.E. Burke, E. Turnbull, *Prog. Met. Phys.* 3 (1952) 220.
- [39] J.L.M. Rupp, A. Infortuna, L.J. Gauckler, *Acta Mater.* 54 (2006) 1721–1730.
- [40] G. Gottstein, L.S. Shvindlerman, *Acta Mater.* 50 (2002) 703–713.
- [41] J. Zhao, Y. Ikuhara, T. Sakuma, *J. Am. Ceram. Soc.* 81 (1998) 2087–2092.
- [42] F. Liu, R. Kirchheim, *Thin Solid Films* 466 (2004) 108–113.
- [43] A. Michels, C.E. Krill, H. Ehrhardt, R. Birringer, D.T. Wu, *Acta Mater.* 47 (1999) 2143–2152.
- [44] T.G. Nieh, *J. Wadsworth, J. Am. Ceram. Soc.* 72 (1989) 1469–1472.
- [45] K. Matsui, H. Horikoshi, N. Ohmichi, M. Ohgai, H. Yoshida, Y. Ikuhara, *J. Am. Ceram. Soc.* 86 (2003) 1401–1408.
- [46] S. Shukla, S. Seal, R. Vij, S. Bandyopadhyay, *Nano Lett.* 3 (2003) 397–401.
- [47] C.W. Kuo, Y.H. Shen, I.M. Hung, S.B. Wen, H.E. Lee, M.C. Wang, *J. Alloy Compd.* 472 (2009) 186–193.
- [48] Z.A. An, H. Ding, Q.P. Meng, Y.H. Rong, *Scripta Mater.* 61 (2009) 1012–1015.
- [49] W.W. Mullins, J. Vinals, *Acta Metall.* 37 (1989) 991–997.
- [50] J.H. Dong, M.Z. Hu, E.A. Payzant, T.R. Armstrong, P.F. Becher, *J. Nanosci. Nanotechnol.* 2 (2002) 161–169.
- [51] J.L.M. Rupp, C. Solenthaler, P. Gasser, U.P. Muecke, L.J. Gauckler, *Acta Mater.* 55 (2007) 3505–3512.
- [52] S. Heiroth, T. Lippert, A. Wokaun, M. Döbeli, *Appl. Phys. A - Mater.* 93 (2008) 639–643.
- [53] S. Heiroth, T. Lippert, A. Wokaun, M. Döbeli, J.L.M. Rupp, B. Scherrer, L.J. Gauckler, *J. Eur. Ceram. Soc.* 30 (2010) 489–495.
- [54] A. Bieberle-Hütter, D. Beckel, A. Infortuna, U.P. Muecke, J.L.M. Rupp, L.J. Gauckler, S. Rey-Mermet, P. Mural, N.R. Bieri, N. Hotz, M.J. Stutz, D. Poulikakos, P. Heeb, P. Müller, A. Bernard, R. Gmür, T. Hocker, *J. Power Sources* 177 (2008) 123–130.
- [55] P.C. Su, C.C. Chao, J.H. Shim, R. Fasching, F.B. Prinz, *Nano Lett.* 8 (2008) 2289–2292.
- [56] R. Radhakrishnan, A.V. Virkar, S.C. Singhal, G.C. Dunham, O.A. Marina, *Actuat. B-Chem.* 105 (2005) 312–321.
- [57] A. Ziehfrennd, W.F. Maier, *Chem. Mater.* 8 (1996) 2721–2729.
- [58] M. Birkholz, *Thin Film Analysis by X-ray Scattering*, Wiley-VCH, Weinheim, 2006.
- [59] W. Kleber, H.-J. Bartsch, J. Bohm, *Einführung in die Kristallographie*, Verlag Technik, Berlin, 1998.
- [60] D.K. Bowen, B.K. Tanner, *X-ray Metrology in Semiconductor Manufacturing*, CRC Press, Taylor and Francis Group, Boca Raton, FL, 2006.
- [61] G.F. Vander Voort, F.J. Warmuth, S.M. Purdy, A. Szirmai, *Metallography — Past, Present, and Future 75th Anniversary Volume*, American Society for Testing and Materials, Philadelphia, PA, 1993.
- [62] R. Stevens, *Zirconia and Zirconia Ceramics*, Magnesium Elektron Ltd, Leeds, UK, 1986.
- [63] O.J. Dura, M.A.L. De la Torre, *J. Phys. D Appl. Phys.* 41 (2008) 6.
- [64] M. Yashima, M. Kakihana, M. Yoshimura, *Solid State Ionics* 86–8 (1996) 1131–1149.
- [65] M. Yashima, K. Ohtake, M. Kakihana, H. Arashi, M. Yoshimura, *J. Phys. Chem. Solids* 57 (1996) 17–24.
- [66] J. Suda, O. Kamishima, J. Kawamura, T. Hattori, T. Sato, *J. Phys. Conference Series* 150 (2009).
- [67] I. Kosacki, V. Petrovsky, H.U. Anderson, P. Colomban, *J. Am. Ceram. Soc.* 85 (2002) 2646–2650.
- [68] E.F. Lopez, V.S. Escibano, M. Panizza, M.M. Carnasciali, G. Busca, *J. Mat. Chem.* 11 (2001) 1891–1897.
- [69] F. Capel, M.A. Banares, C. Moure, P. Duran, *Mater. Lett.* 38 (1999) 331–335.
- [70] P. Peshev, I. Stambolova, S. Vassilev, P. Stefanov, V. Blaskov, K. Starbova, N. Starbova, *Mater. Sci. Eng. B-Solid* 97 (2003) 106–110.
- [71] M. Kitajima, *Crit. Rev. Solid State* 22 (1997) 275–349.
- [72] Z.D. Dohcevic-Mitrovic, M.J. Scepianovic, M.U. Grujic-Brojcin, Z.V. Popovic, S.B. Boskovic, B.M. Matovic, M.V. Zinkevich, F. Aldinger, *Solid State Commun.* 137 (2006) 387–390.
- [73] M. Ortiz, A.A. Pochettino, *J. Nucl. Mater.* 229 (1996) 65–72.
- [74] M. Tanaka, M. Hasegawa, A.F. Dericioglu, Y. Kagawa, *Mater. Sci. Eng. A-Struct.* 419 (2006) 262–268.
- [75] J.E. Spangler, R.D. Robinson, F. Zheng, S.W. Chan, I.P. Herman, *Phys. Rev. B* 64 (2001).
- [76] C.H. Perry, F. Lu, D.W. Liu, B. Alzyab, *J. Raman Spectrosc.* 21 (1990) 577–584.
- [77] A.A. Bukaemskiy, D. Barrier, G. Modolo, *J. Alloy Compd.* 472 (2009) 286–293.
- [78] P.R. Willmott, J.R. Huber, *Rev. Mod. Phys.* 72 (2000) 315–328.
- [79] C.H. Gorbitz, H.P. Hersleth, *Acta Crystall. B-Stru.* 56 (2000) 526–534.
- [80] L. Nichtova, R. Kuzel, Z. Matej, J. Sicha, J. Musil, Z. Kristall, Part 2 (2009) 235–240.
- [81] V. Weidenhof, I. Friedrich, S. Ziegler, M. Wuttig, *J. Appl. Phys.* 89 (2001) 3168–3176.
- [82] X. Wang, M. Rein, J.J. Vlassak, *J. Appl. Phys.* 103 (2008) 6.
- [83] J.Z. Chen, S.K. Wu, *Thin Solid Films* 339 (1999) 194–199.
- [84] M.C. Weinberg, D.P. Birnie III, V.A. Shneidman, *J. Non-Cryst. Solids* 219 (1997) 89–99.
- [85] F.R. Chien, A.H. Heuer, *Philos. Mag. A* 73 (1996) 681–697.
- [86] M. Döbeli, *J. Phys.-Condes. Mat.* 20 (2008) 7.
- [87] M. Mori, Y. Hiei, T. Yamamoto, *J. Am. Ceram. Soc.* 84 (2001) 781–786.
- [88] R.P. Ingel, D. Lewis, *J. Am. Ceram. Soc.* 69 (1986) 325–332.
- [89] K. Shimizu, G.E. Thompson, G.C. Wood, *Thin Solid Films* 77 (1981) 313–318.
- [90] V.V. Roddatis, D.S. Su, F.C. Jentoft, R. Schlogl, *Philos. Mag. A* 82 (2002) 2825–2839.
- [91] B.J. Kooi, W.M.G. Groot, J.T.M. De Hosson, *J. Appl. Phys.* 95 (2004) 924–932.
- [92] A. Meldrum, L.A. Boatner, R.C. Ewing, *J. Mater. Res.* 12 (1997) 1816–1827.
- [93] C. Lou, M.A. Player, *J. Phys. D Appl. Phys.* 35 (2002) 1805–1811.
- [94] B.P. Gorman, V. Petrovsky, H.U. Anderson, T. Petrovsky, *J. Mater. Res.* 19 (2004) 573–578.
- [95] J.A. Thornton, *J. Vac. Sci. Technol. A* 4 (1986) 3059–3065.
- [96] J. Maier, *Z. Phys. Chem.* 217 (2003) 415–436.
- [97] J. Maier, *J. Eur. Ceram. Soc.* 24 (2004) 1251–1257.
- [98] A. Evans, A. Bieberle-Hütter, J.L.M. Rupp, L.J. Gauckler, *J. Power, Sources* 194 (2009) 119–129.
- [99] Y.H. Tang, K. Stanley, J. Wu, D. Ghosh, J.J. Zhang, *J. Micromech. Microeng.* 15 (2005) S185–S192.